Properties of ultrathin molybdenum films for interconnect applications

Valeria Founta[a,b,c,*], Jean-Philippe Soulié[a,*], Kiroubanand Sankaran[a], Kris Vanstreels[a], Karl Opsomer[a], Pierre Morin[a], Pieter Lagrain[a], Alexis Franquet[a], Danielle Vanhaeren[a], Thierry Conard[a], Johan Meersschaut[a], Christophe Detavernier[d], Joris Van de Vondel[c], Ingrid De Wolf[a,b], Geoffrey Pourtois[a], Zsolt Tőkei[a], Johan Swerts[a], and Christoph Adelmann[a,†]

[a] Imec, Kapeldreef 75, 3001 Leuven, Belgium
[b] KU Leuven, Departement Materiaalkunde, Kasteelpark Arenberg 44, 3001 Leuven, Belgium
[c] KU Leuven, Departement Natuurkunde en Sterrenkunde, Celestijnenlaan 200d, 3001 Leuven, Belgium
[d] Universiteit Gent, Department Vastestofwetenschappen, CoCooN, Krijgslaan 281, 9000 Gent, Belgium

Abstract

The structural and electrical properties of Mo thin films with thicknesses between 3 and 50 nm, deposited by physical vapor deposition, have been evaluated in order to assess the potential of Mo as an alternative to Cu for nano-interconnect applications. Mo films deposited on SiO_2/Si were polycrystalline with randomly oriented grains close to the interface and the progressive formation of a (110) texture above 5 nm film thickness. Adhesion between Mo and low-κ dielectrics was strong with an adhesion energy above 5 J/m^2. The Mo resistivity showed a weaker thickness dependence than Cu, which rendered Mo competitive with conventional TaN/Cu/TaN metallization below metal thicknesses of 8 nm. Semiclassical resistivity modeling found that the thin film resistivity was limited by grain boundary scattering. Furthermore, the effects of Mo deposition on different dielectric and metallic substrates and of post-deposition annealing up to 950ºC were investigated. Crystallinity, impurity concentration, and resistivity were all affected by the substrate. Post-deposition annealing in H_2 led to continuous grain growth, followed by recrystallization at 860ºC. By contrast, annealing in H_2/N_2 led to the incorporation of N in the films and ultimately to Ta nitride formation above 500ºC. The results indicate that Mo can be a promising candidate for advanced interconnect metallization schemes if surface oxidation as well as impurity incorporation can be kept under control.

Keywords: Interconnect metallization, thin films, molybdenum, resistivity scaling

1. Introduction

In recent technology nodes, the performance of large-scale integrated circuits has become progressively limited by their interconnects due to strongly increasing line and via resistances as well as to deteriorating reliability [1–8]. Besides unavoidable geometrical effects when line and via cross-sections are reduced, the increase of line and via resistances can be attributed to two root causes: it is known for decades that the resistivity of thin metallic films or nanowires strongly increases at the nanoscale because of increased scattering at rough surfaces or interfaces [9,10] as well as, in polycrystalline metals, by grain boundaries [11,12]. These

---

effects become dominant for line or via dimensions comparable to the mean free path (MFP) of the conductor, which is on the order of (10s of) nm. Since Cu possesses a rather long MFP of around 40 nm [13], these finite size effects are aggravated at current interconnect dimensions around 15 nm and thus recently alternative metals have been intensively researched to identify potential alternatives to Cu with a much lower MFP and thus much lower sensitivity of the resistivity to grain boundary or interface scattering [8,14–16].

Moreover, Cu interconnects require barrier (typically TaN) and liner (typically Ta or Co) layers for reliable operation [4,6,7,17–20]. The thickness of these layers cannot be scaled below certain limits to guarantee their function and therefore, they further reduce the cross-sectional area available for Cu in an interconnect line or via. Barrier and liner layers do not contribute much to the overall conductance due to their relatively high resistance, which further exacerbates the strong line and via resistance increase at reduced dimensions. Consequently, this has led to research on metals that do not require barrier and liner layers for reliable interconnect operation.

For these reasons, alternatives to Cu metallization have been intensively researched in the recent past. An ideal interconnect metal combines low bulk resistivity and a short MFP with a high melting point that can serve as a proxy for reliability, *i.e.,* for the resistance to electromigration and the need for diffusion barriers [21,22]. Hence, recent research has focused on elemental refractory metals with short MFPs, such as Co [23,24] which has recently been introduced into commercial circuits [25,26]. Additional work has addressed the prospects of Pt-group metals [27], especially of Ru [28–33].

In this paper, we present a comprehensive study of Mo thin films from a point of view of an application as alternative metallization in advanced interconnects. Mo is a refractory metal (T_{melt} = 2620°C) with a low coefficient of thermal expansion (α = 4.8×10^{-6} K^{-1}), a low bulk resistivity at room temperature (53.4 nΩm), and an MFP of 11 nm [13], much shorter than the

Cu MFP of 40 nm. Hence, Mo can be considered as a prospective metal for advanced interconnects beyond Cu. Mo thin films have been studied in detail for applications in, *e.g.*, Mo/Si multilayers for soft x-ray optics [34,35], or as electrodes in solar cells [36,37]. However, a comprehensive assessment of Mo for interconnect metallization applications is still lacking. This work attempts to fill this gap by assessing the relevant structural, mechanical, and electrical properties of Mo thin films with thicknesses between 3 and 50 nm that can be used as a proxy for the behavior in scaled interconnect lines and vias. The results indicate that Mo is a promising alternative to replace Cu in interconnect applications if the chemical sensitivity of Mo to its environment can be controlled.

2. Experimental and computational methods

All Mo films were deposited by physical vapor deposition (PVD) on 300 mm Si (100) wafers using a Mo target with a purity of 5N. Prior to PVD, a 100 nm thick thermal SiO_2 was grown to provide electrical insulation. In some cases, when the effect of the substrate on the Mo thin film properties was studied (Sec. 3.3), additional 5 to 8 nm thick layers (TaN, TiN, HfO_2, ZrO_2, Al_2O_3) were deposited onto SiO_2. HfO_2, ZrO_2, Al_2O_3, TiN, and TaN were deposited by atomic layer deposition using $HfCl_4/H_2O$, $ZrCl_4/H_2O$, $Al(CH_3)_3/H_2O$, $TiCl_4/NH_3$, and $TaCl_5/NH_3$ respectively. In some annealing studies, Mo was capped by 3 nm of Ru or TaN, as well as 5 nm of SiN or SiCN. Ru, TaN, and SiN capping layers were deposited by (reactive) PVD, whereas SiCN was deposited by plasma-enhanced chemical vapor deposition. Post-deposition annealing was carried out on 300 mm wafers in an ASM A412 vertical furnace up to temperatures of 600ºC in H_2 or N_2/H_2, as indicated in the text. Additional annealing at higher temperatures in N_2/H_2 was performed on coupons in an AG Heatpulse I RTA rapid thermal annealing chamber.

The crystal structure and the thicknesses of the Mo films were determined by 2θ-ω x-ray diffraction (XRD) and grazing-incidence x-ray diffraction (GIXRD, ω = 0.3°) and x-ray reflectance (XRR), respectively, in a Bruker JVX7300 diffractometer using Cu Kα radiation. Additional information about crystallinity, grain size, and thickness, was obtained by transmission electron microscopy (TEM) using a FEI Titan G2 60-300 operating at 120 kV in the dark-field scanning mode. The room-temperature resistivity of the films was assessed by measuring the sheet resistance (Rs) using a KLA RS100 four-point probe sheet resistance mapper in combination with the XRR film thickness, corrected for the thickness of the surface oxide (assumed to be insulating). The resistivity at cryogenic temperatures was obtained in a Quantum Design Physical Property Measurement System using patterned Hall bars. Atomic force microscopy (AFM) was performed on a Bruker ICON microscope in tapping mode. The film stress was determined from wafer bow measurements using a KLA Aleris 8510 Thin Film Metrology System. Rutherford backscattering spectrometry (RBS) was performed using 1.52 He$^+$ ions at a backscatter angle of 170º. Time-of-flight secondary-ion mass spectrometry (ToF-SIMS) profiles were obtained with an ION-TOF TOF-SIMS V instrument. Both positive and negative ion profiles were measured in a dual beam configuration using a Bi$^+$ (15 keV) gun for analysis and a Cs$^+$ (350 eV) gun for sputtering. X-ray photoelectron spectroscopy (XPS) measurements were carried out in angle-resolved mode using a Theta300 system from Thermo Instruments using a monochromatized Al Kα x-ray source (1486.6 eV) and a measurement spot size of 400 μm.

The Fermi surface of Mo has been obtained by *ab initio* calculations using the DFT Quantum espresso package [38] using a Monkhorst–Pack sampling scheme with a *k*-point density of 60×60×60. The valence electrons are described using the GBRV pseudopotentials [39] within the Perdew–Burke–Ernzerhof generalized gradient approximation [40] with a cut-off of the kinetic energy of 60 Ry, which ensures a convergence within 10^{-12} eV of the total

energy. Based on the Fermi surface, the $\lambda \times \rho_0$ product was calculated using the semiclassical transport approach outlined in Refs. [13,27,41].

3. Results and discussion

The paper is organized as follows. First, the properties of as-deposited ultrathin Mo films on thermally grown SiO_2/Si (100) as a reference substrate are discussed. This section includes the film thickness dependence of the Mo resistivity down to 3 nm and its analysis using semiclassical transport modeling. Next, the effect of different substrates commonly used in semiconductor device applications on the Mo thin film properties is addressed. The third part of the paper then details the effects of post-deposition annealing, including the effect of the annealing ambient. This work thus provides a comprehensive perspective for Mo metallization in advanced semiconductor devices.

3.1. *Microstructural and morphological properties of as deposited Mo films on SiO₂*

All Mo thin films deposited in this work were polycrystalline. Figures 1a and 1b show the 2θ-ω XRD and GIXRD patterns, respectively, of thin Mo films with thicknesses between 5 and 30 nm deposited on SiO_2. In all cases, the patterns are consistent with the stable bcc phase of Mo. The 2θ-ω patterns in Fig. 1a are dominated by a strong (110) reflection with an intensity that rapidly increased with thickness. By contrast, the GIXRD patterns in Fig. 1b show both (110) and (200) reflections with intensities that depend only weakly on the film thickness, somewhat similar to previous reports [42,43]. The thickness dependence of the Mo (110) peak intensities (normalized to the peak intensity for 5 nm film thickness) measured both by GIXRD and 2θ-ω XRD is represented in Fig. 1c. These data quantify the above observations and confirm that the GIXRD (110) peak intensity is nearly independent of thickness whereas the 2θ-ω XRD (110) peak intensity increases over tenfold from 5 nm to 30 nm. The 2θ-ω intensity

increase is much larger than the increase of the scattering volume and can therefore be attributed to an increase in the overall crystallinity (order) of the Mo films.

These observations can be explained by the coexistence of a randomly oriented (rather disordered) minority phase with a highly (110) textured majority phase [44]. In the 2θ-ω XRD scans, only crystallographic planes perpendicular to the surface normal contribute to the diffracted x-ray intensity. By contrast, GIXRD patterns (with $\omega \ll 2\theta$) correspond to crystallographic planes that are inclined by an angle of $\delta \approx 90° - \frac{2\theta}{2}$ with respect to the surface. Hence, 2θ-ω XRD provides information about planes oriented parallel to the surface, while GIXRD characterizes typically randomly oriented grains since δ does in general not correspond to any specific crystallographic direction for textured films for a given 2θ. The thickness-independent GIXRD intensity suggests that the randomly oriented minority phase is formed during initial film nucleation and located at the interface with the SiO_2 substrate. Further deposition leads then to the formation of a strongly (110) oriented textured film, in keeping with the strong dependence of the intensity of the (110) reflection in the 2θ-ω XRD patterns on the film thickness.

This behavior is confirmed by an analysis of the thickness dependence of the Scherrer grain size deduced from both the GIXRD and 2θ-ω XRD patterns. While the grain size of the randomly oriented minority phase deduced from GIXRD is small and rather thickness independent, the Scherrer grain size deduced from 2θ-ω XRD monotonously increases with thickness. This reinforces the picture that the nucleation occurs via randomly oriented grains, followed by texture formation and grain growth, corresponding to the transitional Zone T in the structure zone model [45–48]. In this zone, the growth mode is determined by considerably fast surface diffusion with little bulk or grain boundary diffusion active [46]. Growth starts by initial random nucleation followed by grain coarsening and the successive development of a textured columnar grain structure due to competitive grain growth [48]. It is possible that initial

grain growth is blocked by the incorporation of surface impurities (*e.g.*, O, adventitious C) [46], leading to the highly disordered Mo interface layer evidenced by GIXRD. This will be discussed further in Sec. 3.3.

Figures 2a to 2d show AFM images of as deposited Mo films on SiO_2 with thicknesses between 5 and 50 nm, as indicated. The extracted rms roughness is shown as a function of the film thickness in Fig. 2e. In general, the films were smooth and the rms roughness varied from 0.35 ± 0.04 nm for the 5 nm thick Mo film to 0.63 ± 0.04 nm for the thickest film of 50 nm. Note that the initial SiO_2 rms roughness was around 0.3 nm and hence the thinnest films showed little to no additional roughening with respect to the substrate. Further insight in the evolution of the surface roughness with film thickness could be obtained from the AFM images by determining the lateral correlation length through the autocorrelation function. The results in Fig. 2f indicate some coarsening of the surface structure for thicker films since the lateral correlation length increases from about 10 nm for Mo films below 10 nm (essentially identical to the lateral correlation length of the SiO_2 substrate) to about 20 nm for the 50 nm thick films. This coarsening can be linked to lateral grain growth (see below) in structure Zone T including texture formation and is consistent with the increase of the Scherrer grain size deduced from 2θ-ω XRD (Fig. 1c).

The surface roughness was also determined by XRR (Fig. 3a). XRR confirmed the increase in surface roughness with increasing thickness observed by AFM. Values for the rms surface roughness extracted from XRR (Fig. 3b) were in reasonable agreement with those determined by AFM; small differences can be explained by the different spectral response of AFM and XRR, especially for deviations from Gaussian surface roughness [49]. XRR further revealed that the density of the Mo films was $95\% \pm 3\%$ of the bulk Mo density of 10.3 g/cm^3 for all film thicknesses. The density was confirmed by measuring the Mo area density using RBS.

Combining RBS results with the XRR film thickness (Fig. 4), led to a density of 9.7 ± 0.1 g/cm^3, about 94% of the bulk Mo density.

XRR also revealed the presence of a surface oxide with a thickness of about 2 nm after exposure to air (Fig. 3c). To study the surface oxidation kinetics of Mo, the sheet resistance of a 15 nm thick Mo films was measured as a function of air exposure time at ambient conditions. Assuming that the resistivity does not change with film thickness—which is valid for the small observed thickness changes—the reduction of the sheet resistance can be converted to a reduction of the thickness of the metallic (unoxidized) Mo film that carries the current. The results are shown in Fig. 5a. One can see that the metallic Mo thickness is reduced by about 0.95 nm after a month ($\sim 2.6 \times 10^6$ s). The data also show that the oxidation during the first 24 h ($\sim 10^5$ s) is limited to a metallic Mo loss of about 0.3 nm. This indicates that the Mo surface oxidation is a rather slow process. An analysis of the time dependence assuming a power law dependence $\propto t^\gamma$ (Fig. 5b) shows different kinetics for short times below a few hours (characterized by $\gamma = 0.63 \pm 0.03$) and for longer times (characterized by $\gamma = 0.35 \pm 0.02$). We speculate that this may be due to the formation of an increasingly closed surface oxide layer, which may modify the rate-limiting process from O absorption and surface reactions with Mo to processes including the outdiffusion of Mo to the surface. It should be noted, however, that both exponents differ from the value of $\gamma = 0.5$ expected for pure diffusion processes.

The native oxide of Mo after oxidation in air for a month was analyzed by XPS. The Mo 3d XPS spectrum in Fig. 5c can be accounted for by three components that are attributed to metallic Mo^0 (Mo 3d$_{5/2}$ binding energy of 227.9 eV), Mo^{4+} (Mo 3d$_{5/2}$ binding energy of 231.8 eV), and Mo^{6+} (Mo 3d$_{5/2}$ binding energy of 232.7 eV). The latter two components can be assigned to (different parts) of the surface oxide. Angle-dependence XPS measurements (not shown) suggested that the Mo^{6+} was predominantly found at the surface of the films, whereas

the Mo^{4+} component was situated rather at the interface with Mo^0. The thickness of the native Mo oxide extracted from the XPS measurements by comparing the combined intensity of the Mo^{4+} and Mo^{6+} components to the Mo^0 intensity was 2.7 ± 0.3 nm. This is about $2.8\times$ the thickness of the metallic Mo loss deduced from sheet resistance measurements and can be explained by the volume expansion and the reduction of the Mo atomic density during oxidation. The volume expansion is in reasonable agreement with the atomic density of Mo in MoO_3, which shows that the surface oxide was rather dense.

The built-in stress in the Mo films was determined by wafer bow measurements. Results are depicted in Fig. 6. As deposited ~10 nm thick films showed large tensile stress of the order of 1500 MPa. For thicker films, the stress decreased but still remained on the order of 500 MPa for 30 nm thick films. Large built-in tensile stresses in thin metal films deposited by PVD have typically been linked to the island coalescence process and the formation of grain boundaries at the early nucleation stages of the deposition [50,51]. This is consistent with the XRD results that indicate the formation of a thin nucleation layer with small and randomly oriented crystallites during the initial deposition. Further deposition leads then to the formation of a textured columnar microstructure, which generates incremental compressive stress and reduces tensile stress. This is again a commonly observed stress evolution for the deposition of metallic films and could be interpreted by the progressive incorporation of adatoms into grain boundaries [50–52]. However, the tensile stress remains relatively large, still exceeding 500 MPa for a 30 nm thick film.

Strong adhesion to the surrounding dielectrics is a crucial requirement for the integration of metals into scaled interconnects. Table 1 presents experimental adhesion energies determined using four-point bending on both SiO_2 and dense low-κ organosilicate glass (OSG, κ = 3.0), which is commonly used as a dielectric in interconnects. The adhesion between Mo and the dielectrics was strong with adhesion energies > 5 J/m^2 in all cases. Annealing at high

temperature (800°C) did not affect the adhesion on SiO_2 within the experimental accuracy. Similar to the case of Ru [28], adding a 0.3 nm thick discontinuous TiN adhesion liner already increased the adhesion measurably. However, values of about 5 J/m^2 are typically sufficient to allow for the integration in conventional damascene interconnect processing as well as packaging schemes and therefore no adhesion liners are expected to be required for Mo. This is different from more noble metals, such as, *e.g.*, Pt-group metals (Ru, Ir), which show weak adhesion to dielectrics and typically require adhesion liners [28]. This is a clear advantage of more reactive base metals such as Mo, which may enable fully linerless metallization with associated advantages in line resistance.

3.2. Resistivity scaling of Mo thin films on SiO_2

The resistivity of a metal at small interconnect line and via dimensions is a critical property that determines its promise for interconnect applications. However, the interconnect line and via resistances strongly depend on the detailed metallization scheme and the integration route and are therefore difficult to assess in general. By contrast, the resistivity scaling behavior of thin films is comparatively easy to assess and has thus been often used as a proxy for the "intrinsic" resistivity scaling prospects for interconnects [15,27]. We have therefore determined the thickness-dependent thin film resistivity of as deposited Mo films on SiO_2. The results are shown in Fig. 7. For comparison, thickness-dependent resistivities of W, Ru, and TaN/Cu/TaN thin films [27] are also shown. The TaN/Cu/TaN (1.5 nm TaN/x nm Cu/1.5 nm TaN) can be considered as a simplified equivalent of the metallization scheme used in current interconnects. Prior to the resistivity measurements, the Cu and Ru samples were annealed at 420ºC for 20 min in forming gas to mimic a typical thermal budget during interconnect processing. Annealing W under the same conditions had no measurable effect on the resistivity.

The annealing behavior of Mo and its impact on thin film resistivity will be discussed in more detail in Sec. 3.4 below.

The data show that Mo outperforms W over the entire thickness range and TaN/Cu/TaN below about 8 nm total metal thickness. To shed further light on the resistivity scaling of Mo, the thickness dependence of the resistivity has been modeled within the semiclassical model developed by Mayadas and Shatzkes [12] that considers both surface as well as grain boundary scattering. In this model, the resistivity ρ_{tf} of a polycrystalline thin film with thickness h and linear intercept length between grain boundaries g is given by [12]

$$\rho_{tf} = \left\{ \frac{1}{\rho_{GB}} - \frac{6}{\pi k_0 \rho_0} (1-p) \int_0^{\frac{\pi}{2}} d\varphi \int_1^\infty dt \frac{\cos^2 \varphi}{H^2} \left(\frac{1}{t^3} - \frac{1}{t^5} \right) \frac{1 - e^{-k_0 tH}}{1 - p e^{-k_0 tH}} \right\}^{-1}, \qquad (1)$$

with $H = 1 + \alpha / \left(\cos\varphi \sqrt{(1 - 1/t^2)} \right)$, $k_0 = h/\lambda$, $\alpha = (\lambda/g) \times 2R/(1-R)$, and $\rho_{GB} = \rho_0 [1 - (3\alpha/2) + 3\alpha^2 - 3\alpha^3 \ln(1 + 1/\alpha)]^{-1}$. Here, ρ_0 denotes the bulk resistivity of the metal and λ the bulk mean free path of the charge carriers (due to electron-phonon scattering). Surface scattering is described via the phenomenological parameter $0 \leq p \leq 1$. A value of $p = 1$ corresponds to specular scattering at surfaces or interfaces, whereas $p = 0$ corresponds to fully diffuse scattering. By contrast, grain bounday scattering is characterized by the quantum-mechanical reflection coefficient of the charge carriers from a grain boundary, $0 \leq R \leq 1$.

The mean free path of a metal can be determined from *ab initio* calculations of the electronic structure, as introduced by Gall [13]. It has be shown that, for bulk metals with the bulk resistivity determined by electron-phonon scattering, the product of the mean free path and the bulk resistivity, $\lambda \times \rho_0$, can be approximately written as a function of the Fermi surface morphology only and does not require calculations of electron-phonon relaxation rates. In this framework, the mean free path can then be obtained from *ab initio* calculations of the Fermi surface if the bulk resistivity is known ($\rho_0 = 53.4$ nΩm for Mo). Following the approach

11

detailed in Dutta *et al.* [27], the analysis of the Mo Fermi surface (Fig. 8a) led to a mean free path of $\lambda = 11.2$ nm, in agreement with the results in [13]. We remark that the resistivity of bulk cubic Mo is anisotropic as is the mean free path in this framework [53]. The model further requires the knowledge of the film thickness dependence of the linear intercept length between grain boundaries (related to the grain size [54]). This was extracted from plan-view TEM images (Figs. 8b to 8e) of the films. Figure 8f shows the experimental resistivities as well as the result of the best fit of Eq. (1) to the data. Excellent agreement between the experiment and the model was obtained for fully diffuse surface scattering ($p = 0$) and a grain boundary reflection coefficient of $R = 0.46 \pm 0.03$. The value of R is comparable to that of Ru ($R = 0.43$ to 0.58) or Ir ($R = 0.47 \pm 0.03$) [27], which supports modeling results suggesting that refractory metals are characterized by rather high grain boundary reflection coefficients on the order of $R \sim 0.5$ [55]. We remark that $R \sim 0.20$ to 0.25 for Cu [3,27,56,57].

The above results pose the question whether the thin film resistivity is determined by surface or grain boundary scattering. Yet, Matthiessen's rule does not apply to Eq. (1) and therefore surface and grain boundary scattering contributions cannot be quantitatively separated. Nonetheless, following the arguments in Ref. [27], some insight can be gained by considering the sum of squared residuals (SSR) of modelled and experimental resistivities as a function of model parameters p and R. The resulting graph is depicted in Fig. 8g and shows an elongated SSR minimum along the p direction. This behavior is reminiscent to that of Ru and Ir [27] and indicates that the contribution of surface scattering is rather weak as the variation of p only weakly affects the resistivity (and therefore the SSR). Consequently, the Mo thin film resistivity appears to be dominated by grain boundary scattering, very similar to the findings for Ru and Ir [27]. This suggests that the resistivity of thin films of refractory metals tends to be strongly determined by grain boundary scattering, presumably also due to their large grain boundary reflection coefficients, as well as potentially the difficulty to obtain large grains at

low thermal budgets. Again, for Cu, grain boundary scattering is weaker, and the contribution of surface scattering is therefore stronger for small film thicknesses [3,27,56]. Hence, achieving large grain sizes to reduce the resistivity is even of more paramount importance for refractory metals (such as Mo) than for Cu. Nonetheless, the thickness dependence of the Mo resistivity (as well as that of Ru and Ir) is weaker than that of Cu because of the much smaller mean free path of Mo with respect to Cu.

3.2.1. Temperature dependence of the resistivity of thin Mo films

Further insight into the relative impact of the different scattering mechanisms can be obtained from the temperature dependence of the resistivity [58,59]. The thin film resistivity model expressed by Eq. (1) is not explicitly temperature dependent but rather implicitly via the temperature dependence of the bulk resistivity and the mean free path. As mentioned above, the product of the mean free path and the bulk resistivity, $\lambda \times \rho_0$, is only a function of the Fermi surface morphology and, well below the Fermi temperature of the metal, can be typically assumed to be approximately independent of temperature T. Hence,

$$\lambda(T) \times \rho_0(T) \approx \text{const} \tag{2}$$

For electron-phonon scattering, the temperature dependence of the resistivity is given by the Bloch-Grüneisen law

$$\rho_0(T) = CT^5 \int_0^{\frac{\Theta_D}{T}} \frac{x^5}{(e^x - 1)(1 - e^{-x})} dx, \tag{3}$$

with Θ_D the Debye temperature of the metal and C a prefactor that can, *e.g.*, be determined from the room temperature resistivity. This allows for the calculation of the temperature dependence of the mean free path. The temperature dependences of mean free path and bulk resistivity can then be combined with the semiclassical thin film resistivity in Eq. (1) to calculate its temperature dependence. Here, the surface and grain boundary scattering parameters, p and R, are assumed to be temperature independent.

13

Figure 8h shows the experimental temperature dependence of the resistivity of a 6 nm thin Mo film between T = 10 K and room temperature. Excellent agreement with the model (solid line, Θ_D = 370 K) could be achieved over the entire temperature range using the parameters (p = 0, R = 0.46) obtained by modeling the thickness dependence of the resistivity and a linear intercept length between grain boundaries of 8.2 nm, in reasonable agreement with the experimental value of ~7 nm.

The above approach can also be used to determine the experimental temperature coefficient of the resistivity (TCR). The result is shown in Fig. 8i. The data indicates that the TCR of Mo is close to the bulk value of 0.23 nΩm/K [60], independent of thickness down to about 6 nm. For the thinnest film of 4 nm, a decrease by about 20% was observed. This behavior is very similar to that of Co and Ru reported before [59] and has been ascribed [within the semiclassical thin film resistivity model in Eqs. (1) to (3)] to dominant grain boundary scattering [59], in agreement with the above analysis of the thickness dependence. By contrast, the TCR is expected to increase with decreasing thickness when the resistivity is dominated by surface scattering. The TCR roll-off for the thinnest film has also been observed for Co and Ru [59] and has been ascribed to strongly increased disorder and the breakdown of Matthiessen's rule [59,61,62]. We note that this is in qualitative agreement with the deposition model discussed above, in which the deposition of a randomly oriented nucleation layer (with presumably large disorder) is followed by the deposition of an increasingly crystalline textured film. We further note that the thickness-dependence of the residual resistivity ratio (RRR, Fig. 8i) also corroborates this model. Absolute RRR values are rather small, which can be ascribed to the small grains and the large resulting disorder in the films.

14

3.3. Effects of the substrate on Mo thin film properties

The Mo films reported in the previous section have all been deposited on SiO_2 as a reference substrate. In many microelectronic applications, Mo films are however in contact with different dielectric or metallic substrates. We have therefore also studied the dependence of the Mo thin film properties on other representative dielectric and metallic substrates, such as Al_2O_3, HfO_2, ZrO_2, TiN, and TaN, in addition to SiO_2 reported in the previous section.

Figures 9a and 9b show 2θ-ω XRD and GIXRD patterns of 15 nm thick Mo films on the different substrates, as indicated. The data clearly show that the (110) peak intensities in the 2θ-ω XRD and GIXRD pattern are correlated: strong 2θ-ω XRD intensities are found to correlate with weak GIXRD intensities and *vice versa*. This can be understood within the deposition model discussed above as well as the observation of a Zone T behavior and suggests that films on Al_2O_3, HfO_2, and TaN are more crystalline (and more textured) and contain less disordered interface layers than films on SiO_2, ZrO_2, and TiN.

The difference in crystallinity also has an impact on the Mo thin film resistivity. Figure 9c shows the resistivity of the 15 nm thick films on the different substrates. The resistivity followed in general the trends observed in the XRD pattern. The lowest resistivities were observed for Mo on Al_2O_3, HfO_2, and TaN, whereas the resistivity of Mo on TiN was particularly high. To better understand the effect of the substrate on the resistivity, the impurity concentrations in the Mo films on different substrates were studied by ToF-SIMS. Figures 9d and 9e show the MoO^- and C^- secondary ion yield as a function of sputter time (depth). The data show that the resistivities are clearly correlated with the O and C contents in the bulk of the Mo film. Highest O and C concentrations were present in Mo/TiN, about 6× (for O) and 2× (for C) higher than in Mo/TaN. No other clear correlations between film properties and ToF-SIMS yield (*e.g.*, the N concentration) were observed.

15

The direct correlation between the O content and the resistivity is apparent in Fig. 9f, which shows a monotonous rapid increase of the resistivity as a function of MoO⁻ secondary ion yield. Similar correlations were also observed between MoO⁻ secondary ion yield and the 2θ-ω XRD and GIXRD Mo (110) peak intensities. High O content led to weaker 2θ-ω XRD and larger GIXRD Mo (110) peak intensity. It is challenging to link the increased resistivity directly to impurity scattering as the ToF-SIMS yield cannot be directly quantified. EDS and XPS (not shown) suggest that absolute O concentrations were on the order of the detection limit, *i.e.*, around 1 at.%. It is therefore likely that the resistivity increase rather stems indirectly from the reduced crystallinity and small grain size indicated by the XRD and GIXRD patterns, as it has been shown in the previous section that the Mo thin film resistivity is strongly affected by grain boundary scattering.

Where do the O and C contaminations come from? All Mo films were deposited with the same high purity target (5N) and therefore the contaminants cannot be incorporated directly due to the deposition itself. By contrast, especially the presence of C suggests that the contaminants originate from adventitious surface layers, for example sorbed H_2O or adventitious C that is always present on surfaces exposed to air. As also discussed in the next section, Mo is a reactive metal, and it is therefore likely that weakly bonded atoms on the initial substrate surface can be incorporated into the film. Moreover, Mo may reduce the surface oxide of the substrate layers, especially the surface oxide of TiN. These observations are consistent with the above discussion that the Zone T growth behavior, especially the transition between random nucleation and texture formation, can be affected by the presence of impurities. Such impurities may block grain boundary movement in the first stages of film deposition and lead to a disordered randomly oriented layer at the interface with the substrate. It is plausible that larger impurity concentrations may defer the transition and lead to thicker disordered layers, in agreement with the experimental results.

16

Besides the resistivity, the substrate also strongly affected the stress in the films, as shown in Fig. 9g. As reported above, the built-in stress in Mo/SiO_2 was strongly tensile around 1000 MPa, depending on the film thickness. By contrast, much lower tensile stress was found for Mo/Al_2O_3, and the stress even became (strongly) compressive on HfO_2 and TiN. While the substrate affects nucleation and nuclei coalescence and thus the residual stress formation in the films, the strong compressive stress may also be attributed to impurity incorporation [63–65]. The separation of these direct (impurities) and indirect (microstructure) influences on residual stress in Mo thin films will however require further research.

3.4. Effects of annealing on the properties of Mo thin films

The experimental results in the previous subsections were all obtained on as deposited films. Below, we will address the effect of a post-deposition anneal (PDA) on the properties of Mo thin films. Annealing is a typical step in metallization processing as it tends to increase grain sizes by recrystallization or grain growth [66,67] and typically reduces the resistivity [27,68,69]. It is therefore of great interest to understand the effect of PDAs with different thermal budgets on the microstructure and resistivity of Mo films. A special focus in this work will be on the behavior of annealing temperatures around 420°C since they are relevant for interconnect processing in microelectronic logic applications, although higher annealing temperatures may be allowed when Mo is integrated in (non-volatile) memory applications.

3.4.1. Annealing in N_2/H_2 and Mo nitridation

A typical step in semiconductor processing is the sintering of the structures at temperatures around 420°C in N_2/H_2 (forming gas). Therefore, in a first step, Mo/SiO_2 films were annealed under these conditions (420°C in 80:20 N_2/H_2, atmospheric pressure) and both structural and electrical properties were determined. Somewhat surprisingly, the resistivity was observed to *increase* by about 25% upon annealing, rather independently of the film thickness (Fig. 10a).

This could be attributed to the incorporation of N into Mo during the anneal, as revealed by ToF-SIMS (Fig. 10b) and indicates a high sensitivity of Mo to nitridation even at relatively low temperatures. This will be further discussed below. Note that ToF-SIMS confirmed that the O level in Mo (Fig. 10b) does not increase during annealing (*e.g.,* due to O diffusion from the surface oxide). Hence, the increase in resistivity cannot be attributed to O incorporation.

By contrast, the microstructure of the Mo films and the surface morphology were scarcely affected by the PDA at 420°C in N_2/H_2. Figure 10c shows 2θ-ω XRD pattern of Mo films with different thicknesses between 5 and 30 nm both as deposited and after the PDA. The data indicate that the peak intensities as well as the peak width were not significantly modified. A small downshift of the Mo (110) 2θ peak angle by about 500 arcsec can be attributed to stress relaxation or N incorporation during annealing. Similar results were obtained by GIXRD (data not shown). Moreover, the atomic force micrograph of a 10 nm Mo film in Fig. 10d indicates that the surface morphology was not influenced by the PDA, in keeping with the XRR results (data not shown). The rms roughness deduced to be 0.3 nm and thus identical within experimental accuracy to the value of the as deposited film (see Fig. 2).

While annealing at 420°C did not lead to a phase change of the films, annealing at a higher temperature of 650°C led to the nitridation of the films and the formation of cubic γ-Mo_2N [70,71], as evidenced by the GIXRD pattern in Fig. 10e. The formation of γ-Mo_2N has been observed by ammonolysis in the same temperature range [72,73]. Mo_xN films have also been deposited by reactive sputtering of Mo in an N_2-containing atmosphere [74,75], *i.e.,* under plasma conditions. However, the reaction of Mo with N_2 is thermodynamically favorable and our results show that γ-Mo_2N can occur by the reaction of Mo in N_2/H_2 at relatively low temperatures.

The above results indicate that the annealing of open Mo films in atmospheres containing N_2 (even reducing) should be avoided, even at relatively low temperatures around 400°C,

which are common during interconnect processing. Figure 10f shows the evolution of the Mo thin film resistivity as a function of PDA temperature in an N_2/H_2 ambient. The data indicate that the Mo resistivity starts to increase slightly at temperatures around 400°C, followed by a sharp rise around 550°C that can be attributed to the formation of γ-Mo_2N, in keeping with previous observations of large thin film resistivities of γ-Mo_2N (bulk resistivity about 200 nΩm) [71].

Yet, the data also show that the formation can be avoided by suitable 3 nm thick capping layers that preclude Mo nitridation (see Fig. 10f for 3 nm thick capping layers), either by preventing N indiffusion or Mo outdiffusion towards the surface. The most suitable capping layer appears to be 3 nm of SiN that inhibits nitridation up to 800°C, was well as TaN (up to 700°C). By contrast, Ru does not seem to be a suitable capping layer since it does not delay the onset of the resistivity increase. A decrease in resistivity above 600°C can be attributed to a solid-state reaction and the formation of a Mo-Ru-N intermetallic compound. We note that the resistivity of the SiN and TaN capped samples decreases slowly with annealing temperature due to grain growth, as discussed further below. This is also evidenced by the TEM images in Figs 10g and 10h. A comparison of grain sizes between a 20 nm thick as-deposited (Fig. 10g) and a TaN capped and annealed (at 650°C, Fig10h) sample demonstrates that the grain size indeed increases by annealing. However, the grain growth is limited when compared to an uncapped sample (see next section), which suggests that the capping layer hinders grain growth, *e.g.*, by restricting the movement of grain boundaries.

3.4.2. Microstructural evolution of Mo thin films upon post-deposition annealing

To study the intrinsic annealing behavior of Mo, it is thus mandatory to anneal in an N-free ambient. In order to assess the microstructural evolution of Mo, IS-XRD (Fig. 11a) was performed on a 20 nm thick film (on SiO_2) in an H_2/He atmosphere. Additional measurements

for other film thicknesses between 5 and 30 nm did not show a significantly different behavior and the results below can therefore be assumed to be independent of the Mo thin film thickness (at least within the studied range). The measurements indicated a weak and slow increase of the XRD intensity (which can be linked to an increase of the overall crystallinity and the grain size) in Fig. 11b up to a temperature of around 800°C, followed by a sharp intensity rise that can be linked to a recrystallization process [66,67]. Here, the recrystallization temperature was around 860°C. Such a high recrystallization temperature is consistent with the high melting temperature and large cohesive energy of Mo [66,67]. We note that a similar recrystallization process has been observed for thin Ru films [76], albeit at much lower temperatures around 470°C. Hence, Ru (and more generally Pt-group metals [76]) show much lower recrystallization temperatures than Mo, despite similar melting temperatures, which renders them more susceptible to an increased grain size and a reduced resistivity after PDAs at temperatures compatible with interconnect processing.

The Scherrer grain size in Fig. 11c confirms the above behavior, indicating steady grain growth below 800°C with signs of saturation, followed by a second grain size increase during the recrystallization process up to values close to the film thickness. The grain growth during the first stage of annealing below 800°C was corroborated by the TEM images in Fig. 11d and 11e, that indicated an increase of the average grain size after annealing at 650°C in H_2. Note that the grain size of the annealed (uncapped) sample (at 650°C) is markedly larger than that for the TaN capped sample (annealed at the same temperature) in Fig. 10h, which confirms that the presence of the cap reduces grain growth during annealing. We remark that the resistivity of a 20 nm Mo film after annealing at 650°C in H_2 was 116 ± 5 nΩm and therefore slightly lower than of the TaN-capped samples (128 ± 5 nΩm at 650°C in H_2, further reduced to 120 ± 5 nΩm at 800°C) annealed at a much higher temperature of 800°C. An as-deposited uncapped 20 nm thick Mo film had a resistivity of 136 ± 6 nΩm.

Finally, Fig. 11f present the variation of the out-of-plane lattice parameter c (with respect to the room temperature bulk Mo lattice parameter c_0) of a 20 nm thick Mo film during ramp annealing/cooling up to 950°C and back to room temperature. The data are consistent with the large tensile strain (~500MPa to 1 GPa) observed by wafer bow measurements (Fig. 6). Overall, the out-of-plane lattice parameter increased steadily with temperature due to thermal expansion of the Mo film (and the Si) substrate. Yet, two deviations from the thermal expansion trendline were observed: first, a deviation towards larger values (more compressive stress) around 470°C and a second deviation back towards more tensile stress around 600°C, as evidenced by drastic dc/dT slope changes. This behavior is consistent with wafer bow measurements after cooldown (Fig. 6). A PDA at an intermediate temperature of 420°C led to the formation of strong compressive stress of up to -500 GPa. At an even higher annealing temperature of 650°C, the stress changed back again to tensile, in agreement with the IS-XRD analysis. The data in Fig. 11f further indicate that the cooldown did not introduce any further stress relaxation or change, since the out-of-plane lattice parameter followed the thermal expansion trend line. While the data in Figs. 6 and 11f are qualitatively consistent, the absolute critical temperatures for the stress relaxation mechanisms appear to deviate somewhat. Yet, Fig. 11f represents data obtained during ramp annealing, whereas Fig. 6 was obtained after an extended PDA, which may explain differences in the exact temperature behavior by kinetic effects. This, as well as the underlying stress relaxation processes, requires further study to fully understand the thermal stress behavior of Mo thin films.

4. Conclusions

In conclusion, we have investigated the structural, mechanical, and electrical properties of PVD Mo thin films with thicknesses between 3 and 50 nm for the potential use of Mo as a metal in advanced microelectronic interconnects. The data indicate that Mo is a promising

metal to replace W and even Cu in future interconnect nodes. Due to its short mean free path of the charge carriers (11 nm), the Mo resistivity shows a much weaker thickness dependence than Cu (mean free path of 40 nm). As a result, the Mo resistivity can rival with that of Cu at scaled dimensions (film thicknesses in this work), in particular if Mo does not require barrier and liner layers for reliable operation. Cu metallization schemes require both diffusion barrier and liner layers to prevent from Cu diffusion in the surrounding dielectrics as well as electromigration issues. Since the thickness of barrier and liner layers cannot be reduced below certain limits without losing their function, barrierless metallization schemes can use larger volumes for the conductor metal and therefore provide lower line and via resistances than possible for Cu metallization [15]. In this work, this is mimicked by comparing Mo to TaN/Cu/TaN stacks as proxies of current interconnect metallization and demonstrates that Mo has indeed the potential to replace such stacks with gains in line and via resistance.

The main challenge of Mo as an interconnect metal is its reactivity and its sensitivity to the environment. Mo oxidizes readily in air, leading to insulating surface oxides that can reduce the current-carrying volume in integrated interconnects fabricated by subtractive etch schemes [33]. Annealing in N_2-containing atmospheres can lead to nitridation and resistivity increase even at comparatively low temperatures. The incorporation of surface contaminants can lead to a strong dependence of the Mo properties on the surrounding materials and the substrate for deposition. Hence, Mo metallization schemes need to carefully consider such potential issues to avoid contamination and enable high purity Mo metallization in the interconnect structures.

It is instructive to compare Mo to more noble metals, such as Ru or Ir, from an interconnect performance viewpoint. Both Mo and Ru possess a small mean free path and show a rather similar resistivity scaling behavior due to short mean free paths of the charge carriers. All metals are refractory and can be expected to show excellent reliability behavior in scaled interconnect lines. Ru recrystallizes at a much lower temperature than Mo and thus the Ru

resistivity can be reduced by PDAs, leading to low resistivities especially for Ru metallization by atomic layer deposition [28]. Noble Ru (and Ir) is much more inert than Mo, leading to a much-reduced sensitivity to further processing steps as well as the surrounding materials. However, the relative inertness of Ru and Ir leads to weak adhesion with adjacent dielectrics. While this can be mitigated for Ru by a rather thin TiN adhesion liner that leads only to a small reduction of the available volume for Ru [28], this is much more of an issue for Ir. As shown above, the more reactive nature of Mo results in strong adhesion and therefore adhesion liners are not required. While the above considerations clearly show the relevant trade-offs for different metals in terms of materials properties and resulting interconnect performance, other factors such as cost and process maturity will also strongly affect the choice of the interconnect metal beyond Cu. This is however beyond the scope of the current paper.

CRediT authorship contribution statement

V. Founta: conceptualization, investigation, visualization, writing - original draft; **J.-P. Soulié**: conceptualization, formal analysis, investigation, visualization, writing - review & editing; **K. Sankaran**: conceptualization, methodology, software, formal analysis, writing - review & editing; **K. Vanstreels**: investigation; **P. Morin**: methodology; **P. Lagrain**: investigation; **A. Franquet**: formal analysis, investigation; **D. Vanhaeren**: investigation; **T. Conard**: formal analysis; **J. Meersschaut**: formal analysis, investigation; **J. Van de Vondel**: conceptualization, resources, supervision, writing - review & editing; **I. De Wolf**: conceptualization, supervision, writing - review & editing; **G. Pourtois**: conceptualization, methodology, resources, supervision, writing - review & editing; **Zs. Tőkei**: conceptualization, funding, resources, writing - review & editing; **J. Swerts**: conceptualization, resources, writing

- review & editing; **C. Adelmann**: conceptualization, methodology, formal analysis, resources, supervision, visualization, writing - original draft.

Acknowledgements

References

[1]   P. Kapur, J.P. McVittie, K.C. Saraswat, Technology and reliability constrained future copper interconnects. I. Resistance modeling, IEEE Trans. Electron Devices 49 (2002) 590–597.

[2]   J.D. Meindl, Beyond Moore's Law: the interconnect era, Comput. Sci. Eng. 5 (2003) 20–24.

[3]   D. Josell, S.H. Brongersma, Z. Tőkei, Size-Dependent resistivity in nanoscale interconnects, Annu. Rev. Mater. Res. 39 (2009) 231–254.

[4]   M.R. Baklanov, C. Adelmann, L. Zhao, S.D. Gendt, Advanced interconnects: materials, processing, and reliability, ECS J. Solid State Sci. Technol. 4 (2014) Y1–Y4.

[5]   J.S. Clarke, C. George, C. Jezewski, A. Maestre Caro, D. Michalak, J. Torres, Process technology scaling in an increasingly interconnect dominated world, 2014 IEEE Symp. VLSI Technol. (2014) 142–143.

[6]   Z. Tőkei, I. Ciofi, P. Roussel, P. Debacker, P. Raghavan, M.H. van der Veen, N. Jourdan, C.J. Wilson, V. Vega Gonzalez, C. Adelmann, L. Wen, K. Croes, O. Varela Pedreira, K. Moors, M. Krishtab, S. Armini, J. Bömmels, On-chip interconnect trends, challenges and solutions: how to keep RC and reliability under control, 2016 IEEE Symp. VLSI Technol. (2016): pp. 182–183.

[7]   Z. Tőkei, V. Vega, G. Murdoch, M. O'Toole, K. Croes, R. Baert, M. van der Veen, C. Adelmann, J.P. Soulié, J. Boemmels, C. Wilson, S.H. Park, K. Sankaran, G. Pourtois, J. Sweerts, S. Paolillo, S. Decoster, M. Mao, F. Lazzarino, J. Versluijs, V. Blanco, M. Ercken, E. Kesters, Q.-T. Le, F. Holsteyns, N. Heylen, L. Teugels, K. Devriendt, H. Struyf, P. Morin, N. Jourdan, S. Van Elshocht, I. Ciofi, A. Gupta, H. Zahedmanesh, K. Vanstreels, M.H. Na, Inflection points in interconnect research and trends for 2 nm and beyond in order to solve the RC bottleneck, 2020 IEEE Intern. Electron Devices Meet. (2020) 32.2.1-32.2.4.

[8]   D. Gall, The resistivity bottleneck: the search for new interconnect metals, 2020 Intern. Symp. VLSI Technol. Syst. Applicat. (2020) 112–113.

[9]   K. Fuchs, The conductivity of thin metallic films according to the electron theory of metals, Math. Proc. Cambridge Philos. Soc. 34 (1938) 100–108.

[10]   E.H. Sondheimer, The mean free path of electrons in metals, Adv. Phys. 1 (1952) 1–42.

[11]   A.F. Mayadas, M. Shatzkes, J.F. Janak, Electrical resistivity model for polycrystalline films: the case of specular reflection at external surfaces, Appl. Phys. Lett. 14 (1969) 345–347.

[12]   A.F. Mayadas, M. Shatzkes, Electrical-resistivity model for polycrystalline films: the case of arbitrary reflection at external surfaces, Phys. Rev. B. 1 (1970) 1382–1389.

[13]   D. Gall, Electron mean free path in elemental metals, J. Appl. Phys. 119 (2016) 085101.

[14]   C. Adelmann, L.G. Wen, A.P. Peter, Y.K. Siew, K. Croes, J. Swerts, M. Popovici, K. Sankaran, G. Pourtois, S. Van Elshocht, J. Bömmels, Z. Tőkei, Alternative metals for advanced interconnects, 2014 IEEE Intern. Interconnect Technol. Conf. (2014) 173–176.

[15]   C. Adelmann, K. Sankaran, S. Dutta, A. Gupta, S. Kundu, G. Jamieson, K. Moors, N. Pinna, I. Ciofi, S. Van Eishocht, J. Bömmels, G. Boccardi, C.J. Wilson, G. Pourtois, Z. Tőkei, Alternative metals: from *ab initio* screening to calibrated narrow line models, 2018 IEEE Intern. Interconnect Technol. Conf. (2018) 154–156.

[16]   D. Gall, The search for the most conductive metal for narrow interconnect lines, J. Appl. Phys. 127 (2020) 050901.

[17]   C.S. Hau-Riege, An introduction to Cu electromigration, Microelectron. Reliab. 44 (2004) 195–205.

[18]   A.S. Oates, Strategies to ensure electromigration reliability of Cu/low-k interconnects at 10 nm, ECS J. Solid State Sci. Technol. 4 (2014) N3168.

[19]   A.S. Oates, Will reliability limit Moore's Law?, 2014 IEEE Intern. Electron Devices Meet. (2014) 20.7.1-20.7.4.

[20]   K. Croes, C. Adelmann, C.J. Wilson, H. Zahedmanesh, O. Varela Pedreira, C. Wu, A. Leśniewska, H. Oprins, S. Beyne, I. Ciofi, D. Kocaay, M. Stucchi, Z. Tőkei, Interconnect metals beyond copper: reliability challenges and opportunities, 2018 IEEE Intern. Electron Devices Meet. (2018) 5.3.1-5.3.4.

[21]   K. Sankaran, S. Clima, M. Mees, G. Pourtois, Exploring alternative metals to Cu and W for interconnect applications using automated first-principles simulations, ECS J. Solid State Sci. Technol. 4 (2014) N3127–N3133.

[22]   K. Sankaran, S. Clima, M. Mees, C. Adelmann, Z. Tőkei, G. Pourtois, Exploring alternative metals to Cu and W for interconnects: an *ab initio* insight, 2014 IEEE Intern. Interconnect Technol. Conf. (2014) 193–196.

[23]   J. Kelly, J.H.-C. Chen, H. Huang, C.K. Hu, E. Liniger, R. Patlolla, B. Peethala, P. Adusumilli, H. Shobha, T. Nogami, T. Spooner, E. Huang, D. Edelstein, D. Canaperi, V. Kamineni, F. Mont, S. Siddiqui, Experimental study of nanoscale Co damascene BEOL interconnect structures, 2016 IEEE Intern. Interconnect Technol. Conf. (2016) 40–42.

[24]   S. Dutta, S. Beyne, A. Gupta, S. Kundu, S. Van Elshocht, H. Bender, G. Jamieson, W. Vandervorst, J. Bömmels, C.J. Wilson, Z. Tőkei, C. Adelmann, Sub-100 nm^2 cobalt interconnects, IEEE Electron Device Lett. 39 (2018) 731–734.

[25]   C. Auth, A. Aliyarukunju, M. Asoro, D. Bergstrom, V. Bhagwat, J. Birdsall, N. Bisnik, M. Buehler, V. Chikarmane, G. Ding, Q. Fu, H. Gomez, W. Han, D. Hanken, M. Haran, M. Hattendorf, R. Heussner, H. Hiramatsu, B. Ho, S. Jaloviar, I. Jin, S. Joshi, S. Kirby, S. Kosaraju, H. Kothari, G. Leatherman, K. Lee, J. Leib, A. Madhavan, K. Marla, H. Meyer, T. Mule, C. Parker, S. Parthasarathy, C. Pelto, L. Pipes, I. Post, M. Prince, A. Rahman, S. Rajamani, A. Saha, J.D. Santos, M. Sharma, V. Sharma, J. Shin, P. Sinha, P. Smith, M. Sprinkle, A.S. Amour, C. Staus, R. Suri, D. Towner, A. Tripathi, A. Tura, C. Ward, A. Yeoh, A 10 nm high performance and low-power CMOS technology featuring 3rd generation FinFET transistors, self-aligned quad patterning, contact over active gate and cobalt local interconnects, 2017 IEEE Intern. Electron Devices Meet. (2017) 29.1.1-29.1.4.

[26]   F. Griggio, J. Palmer, F. Pan, N. Toledo, A. Schmitz, I. Tsameret, R. Kasim, G. Leatherman, J. Hicks, A. Madhavan, J. Shin, J. Steigerwald, A. Yeoh, C. Auth, Reliability of dual-damascene local interconnects featuring cobalt on 10 nm logic technology, 2018 IEEE Intern. Reliab. Phys. Symp. (2018) 6E.3-1-6E.3–5.

[27]   S. Dutta, K. Sankaran, K. Moors, G. Pourtois, S. Van Elshocht, J. Bömmels, W. Vandervorst, Z. Tőkei, C. Adelmann, Thickness dependence of the resistivity of platinum-group metal thin films, J. Appl. Phys. 122 (2017) 025107.

[28]   L.G. Wen, P. Roussel, O. Varela Pedreira, B. Briggs, B. Groven, S. Dutta, M.I. Popovici, N. Heylen, I. Ciofi, K. Vanstreels, F.W. Østerberg, O. Hansen, D.H. Petersen, K. Opsomer, C. Detavernier, C.J. Wilson, S. Van Elshocht, K. Croes, J. Bömmels, Z. Tőkei, C. Adelmann, Atomic layer deposition of ruthenium with TiN interface for sub-10 nm advanced interconnects beyond copper, ACS Appl. Mater. Interfaces 8 (2016) 26119–26125.

[29]   X. Zhang, H. Huang, R. Patlolla, W. Wang, F.W. Mont, J. Li, C.-K. Hu, E.G. Liniger, P.S. McLaughlin, C. Labelle, E.T. Ryan, D. Canaperi, T. Spooner, G. Bonilla, D. Edelstein, Ruthenium interconnect resistivity and reliability at 48 nm pitch, 2016 IEEE Intern. Interconnect Technol. Conf. (2016) 31–33.

[30]   L.G. Wen, C. Adelmann, O. Varela Pedreira, S. Dutta, M. Popovici, B. Briggs, N. Heylen, K. Vanstreels, C.J. Wilson, S. Van Elshocht, K. Croes, J. Bömmels, Z. Tőkei, Ruthenium metallization for advanced interconnects, 2016 IEEE Intern. Interconnect Technol. Conf. (2016) 34–36.

[31] S. Dutta, S. Kundu, A. Gupta, G. Jamieson, J.F. Gomez Granados, J. Bömmels, C.J. Wilson, Z. Tőkei, C. Adelmann, Highly scaled ruthenium interconnects, IEEE Electron Device Lett. 38 (2017) 949–951.

[32] S. Dutta, K. Moors, M. Vandemaele, C. Adelmann, Finite size effects in highly scaled ruthenium interconnects, IEEE Electron Device Lett. 39 (2018) 268–271.

[33] D. Wan, S. Paolillo, N. Rassoul, B.K. Kotowska, V. Blanco, C. Adelmann, F. Lazzarino, M. Ercken, G. Murdoch, J. Bömmels, C.J. Wilson, Z. Tőkei, Subtractive etch of ruthenium for sub-5nm interconnect, 2018 IEEE Intern. Interconnect Technol. Conf. (2018) 10–12.

[34] D.G. Stearns, R.S. Rosen, S.P. Vernon, Fabrication of high-reflectance Mo–Si multilayer mirrors by planar-magnetron sputtering, J. Vac. Sci. Technol. A 9 (1991) 2662–2669.

[35] S. Braun, H. Mai, M. Moss, R. Scholz, A. Leson, Mo/Si multilayers with different barrier layers for applications as extreme ultraviolet mirrors, Jpn. J. Appl. Phys. 41 (2002) 4074.

[36] M. Jubault, L. Ribeaucourt, E. Chassaing, G. Renou, D. Lincot, F. Donsanti, Optimization of molybdenum thin films for electrodeposited CIGS solar cells, Sol. Energy Mater. Sol. Cells 95 (2011) S26–S31.

[37] Z.-H. Li, E.-S. Cho, S.J. Kwon, Molybdenum thin film deposited by in-line DC magnetron sputtering as a back contact for Cu(In,Ga)Se$_2$ solar cells, Appl. Surf. Sci. 257 (2011) 9682–9688.

[38] P. Giannozzi, S. Baroni, N. Bonini, M. Calandra, R. Car, C. Cavazzoni, D. Ceresoli, G.L. Chiarotti, M. Cococcioni, I. Dabo, A.D. Corso, S. de Gironcoli, S. Fabris, G. Fratesi, R. Gebauer, U. Gerstmann, C. Gougoussis, A. Kokalj, M. Lazzeri, L. Martin-Samos, N. Marzari, F. Mauri, R. Mazzarello, S. Paolini, A. Pasquarello, L. Paulatto, C. Sbraccia, S. Scandolo, G. Sclauzero, A.P. Seitsonen, A. Smogunov, P. Umari, R.M. Wentzcovitch, QUANTUM ESPRESSO: a modular and open-source software project for quantum simulations of materials, J. Phys.: Condens. Matter. 21 (2009) 395502.

[39] K.F. Garrity, J.W. Bennett, K.M. Rabe, D. Vanderbilt, Pseudopotentials for high-throughput DFT calculations, Comput. Mater. Sci. 81 (2014) 446–452.

[40] J.P. Perdew, K. Burke, M. Ernzerhof, Generalized gradient approximation made simple, Phys. Rev. Lett. 77 (1996) 3865–3868.

[41] K. Sankaran, K. Moors, Z. Tőkei, C. Adelmann, G. Pourtois, *Ab initio* screening of metallic MAX ceramics for advanced interconnect applications, Phys. Rev. Mater. 5 (2021) 056002.

[42] D.P. Adams, L.J. Parfitt, J.C. Bilello, S.M. Yalisove, Z.U. Rek, Microstructure and residual stress of very thin Mo films, Thin Solid Films 266 (1995) 52–57.

[43]   A.M. Hofer, J. Schlacher, J. Keckes, J. Winkler, C. Mitterer, Sputtered molybdenum films: Structure and property evolution with film thickness, Vacuum 99 (2014) 149–152.

[44]   T.J. Vink, M.A.J. Somers, J.L.C. Daams, A.G. Dirks, Stress, strain, and microstructure of sputter-deposited Mo thin films, J. Appl. Phys. 70 (1991) 4301–4308.

[45]   R. Messier, A.P. Giri, R.A. Roy, Revised structure zone model for thin film physical structure, J. Vac. Sci. Technol. A 2 (1984) 500–503.

[46]   P.B. Barna, M. Adamik, Fundamental structure forming phenomena of polycrystalline films and the structure zone models, Thin Solid Films 317 (1998) 27–33.

[47]   C.V. Thompson, Structure evolution during processing of polycrystalline films, Annu. Rev. Mater. Sci. 30 (2000) 159–190.

[48]   I. Petrov, P.B. Barna, L. Hultman, J.E. Greene, Microstructural evolution during film growth, J. Vac. Sci. Technol. A 21 (2003) S117–S128.

[49]   V.L. Mironov, O.G. Udalov, B.A. Gribkov, A.A. Fraerman, Comparative x-ray reflectometry and atomic force microscopy of surfaces with non-Gaussian roughness, J. Appl. Phys. 104 (2008) 064301.

[50]   E. Chason, M. Karlson, J.J. Colin, D. Magnfält, K. Sarakinos, G. Abadias, A kinetic model for stress generation in thin films grown from energetic vapor fluxes, J. Appl. Phys. 119 (2016) 145307.

[51]   G. Abadias, E. Chason, J. Keckes, M. Sebastiani, G.B. Thompson, E. Barthel, G.L. Doll, C.E. Murray, C.H. Stoessel, L. Martinu, Stress in thin films and coatings: current status, challenges, and prospects, J. Vac. Sci. Technol. A 36 (2018) 020801.

[52]   E. Chason, B.W. Sheldon, L.B. Freund, J.A. Floro, S.J. Hearne, Origin of compressive residual stress in polycrystalline thin films, Phys. Rev. Lett. 88 (2002) 156103.

[53]   K. Moors, K. Sankaran, G. Pourtois, C. Adelmann, First principles-based screening method for resistivity scaling of anisotropic metals, arXiv:2111.11121 [cond-mat.mtrl-sci] (2021).

[54]   A. Thorvaldsen, The intercept method - 2. Determination of spatial grain size, Acta Mater. 45 (1997) 595–600.

[55]   Y.F. Zhu, X.Y. Lang, W.T. Zheng, Q. Jiang, Electron scattering and electrical conductance in polycrystalline metallic films and wires: impact of grain boundary scattering related to melting point, ACS Nano 4 (2010) 3781–3788.

[56]   J.S. Chawla, F. Gstrein, K.P. O'Brien, J.S. Clarke, D. Gall, Electron scattering at surfaces and grain boundaries in Cu thin films and wires, Phys. Rev. B 84 (2011) 235423.

[57] K. Barmak, A. Darbal, K.J. Ganesh, P.J. Ferreira, J.M. Rickman, T. Sun, B. Yao, A.P. Warren, K.R. Coffey, Surface and grain boundary scattering in nanometric Cu thin films: a quantitative analysis including twin boundaries, J. Vac. Sci. Technol. A 32 (2014) 061503.

[58] C. Adelmann, On the extraction of resistivity and area of nanoscale interconnect lines by temperature-dependent resistance measurements, Solid State Electron. 152 (2019) 72–80.

[59] M. Siniscalchi, D. Tierno, K. Moors, Z. Tőkei, C. Adelmann, Temperature-dependent resistivity of alternative metal thin films, Appl. Phys. Lett. 117 (2020) 043104.

[60] J. Bass, Pure metal resistivities at T= 273.2 K, in: K.-H. Hellwege, J.L. Olsen (Eds.), Electrical Resistivity, Kondo and Spin Fluctuation Systems, Spin Glasses and Thermopower, Springer, Berlin Heidelberg 1983: pp. 5–13.

[61] J.H. Mooij, Electrical conduction in concentrated disordered transition metal alloys, Phys. Status Solidi A 17 (1973) 521–530.

[62] P.A. Lee, T.V. Ramakrishnan, Disordered electronic systems, Rev. Mod. Phys. 57 (1985) 287–337.

[63] P.M. Alexander, R.W. Hoffman, Effect of impurities on intrinsic stress in thin Ni films, J. Vac. Sci. Technol. 13 (1976) 96–98.

[64] H. Windischmann, Intrinsic stress in sputter-deposited thin films, Crit. Rev. Solid State Mater. Sci. 17 (1992) 547–596.

[65] L.P. Kendig, Z.U. Rek, S.M. Yalisove, J.C. Bilello, The role of impurities and microstructure on residual stress in nanoscale Mo films, Surf. Coat. Technol. 132 (2000) 124–129.

[66] F.J. Humphreys, A unified theory of recovery, recrystallization and grain growth, based on the stability and growth of cellular microstructures - I. The basic model, Acta Mater. 45 (1997) 4231–4240.

[67] F.J. Humphreys, M. Hatherly, Recrystallization and Related Annealing phenomena, second edition, Elsevier, Oxford, 2004.

[68] K. Barmak, A. Gungor, C. Cabral Jr., J.M.E. Harper, Annealing behavior of Cu and dilute Cu-alloy films: precipitation, grain growth, and resistivity, J. Appl. Phys. 94 (2003) 1605–1616.

[69] T. Sun, B. Yao, A.P. Warren, K. Barmak, M.F. Toney, R.E. Peale, K.R. Coffey, Surface and grain-boundary scattering in nanometric Cu films, Phys. Rev. B. 81 (2010) 155454.

[70] H. Jehn, P. Ettmayer, The molybdenum-nitrogen phase diagram, J. Less Common Met. 58 (1978) 85–98.

[71] I. Jauberteau, A. Bessaudou, R. Mayet, J. Cornette, J.L. Jauberteau, P. Carles, T. Merle-Méjean, Molybdenum nitride films: crystal structures, synthesis, mechanical, electrical and some other properties, Coatings 5 (2015) 656–687.

[72] M.J. Kim, D.M. Brown, W. Katz, Molybdenum nitride film formation, J. Electrochem. Soc. 130 (1983) 1196–1200.

[73] D. Mckay, J.S.J. Hargreaves, J.L. Rico, J.L. Rivera, X.-L. Sun, The influence of phase and morphology of molybdenum nitrides on ammonia synthesis activity and reduction characteristics, J. Solid State Chem. 181 (2008) 325–333.

[74] P. Hones, N. Martin, M. Regula, F.L. Lévy, Structural and mechanical properties of chromium nitride, molybdenum nitride, and tungsten nitride thin films, J. Phys. D: Appl. Phys. 36 (2003) 1023–1029.

[75] L. Stöber, J.P. Konrath, V. Haberl, F. Patocka, M. Schneider, U. Schmid, Nitrogen incorporation in sputter deposited molybdenum nitride thin films, J. Vac. Sci. Technol. A 34 (2016).

[76] S. Dutta, Finite Size Effects in Platinum-group Metal Nanostructures, PhD thesis, KU Leuven, Leuven 2018.

Table 1: Adhesion energies from four-point bending measurements of Mo thin films on SiO_2 and OSG 3.0 low-κ substrates for different liners and annealing conditions.

Substrate	Adhesion liner	PDA conditions	Adhesion energy (J/m^2)
SiO_2	none	none	6.9 ± 0.5
SiO_2	none	800°C	6.6 ± 0.7
SiO_2	0.3 nm TiN	none	10.1 ± 3.7
OSG 3.0	none	none	5.1 ± 0.5
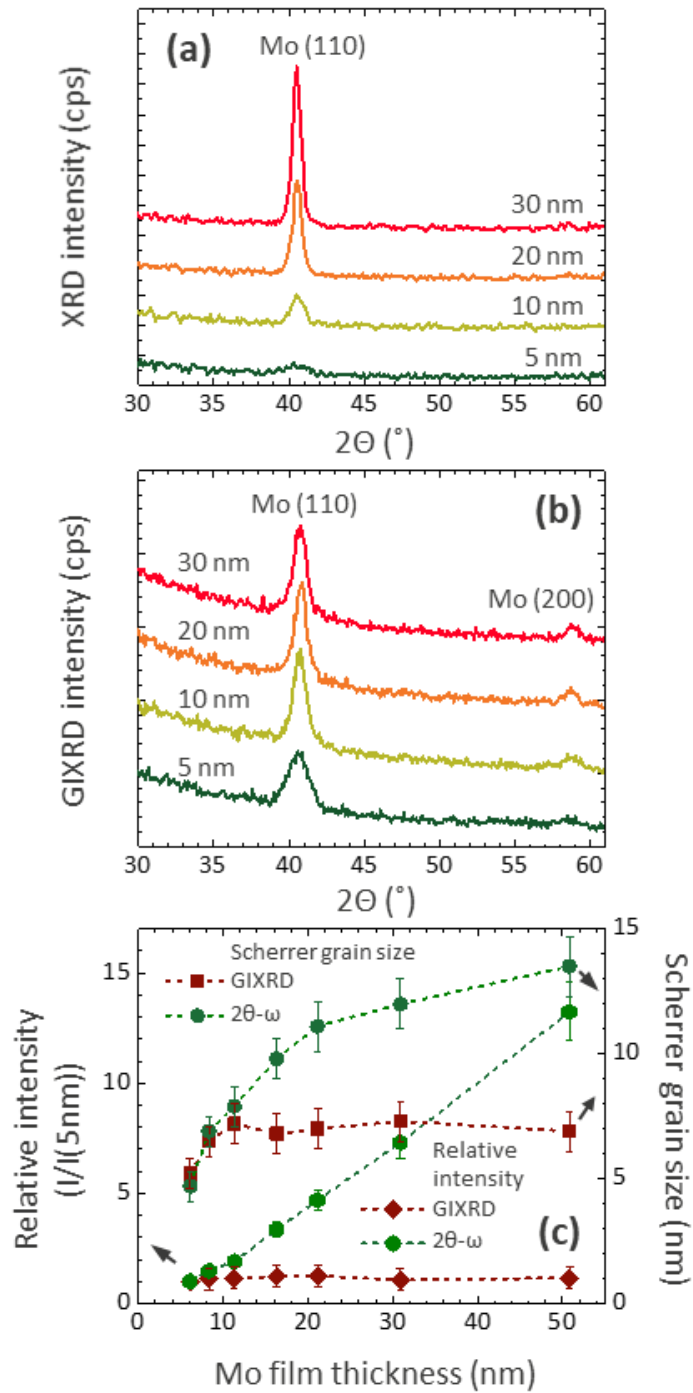
Figure 1: Microstructure of thin Mo films: **(a)** 2θ-ω XRD and **(b)** GIXRD patterns of as-deposited Mo films with thicknesses between 5 and 30 nm as indicated. **(c)** 2θ-ω XRD and GIXRD Mo (110) peak intensity (normalized to the intensity for the 5 nm thick film) as well as Scherrer grain size as a function of Mo film thickness.
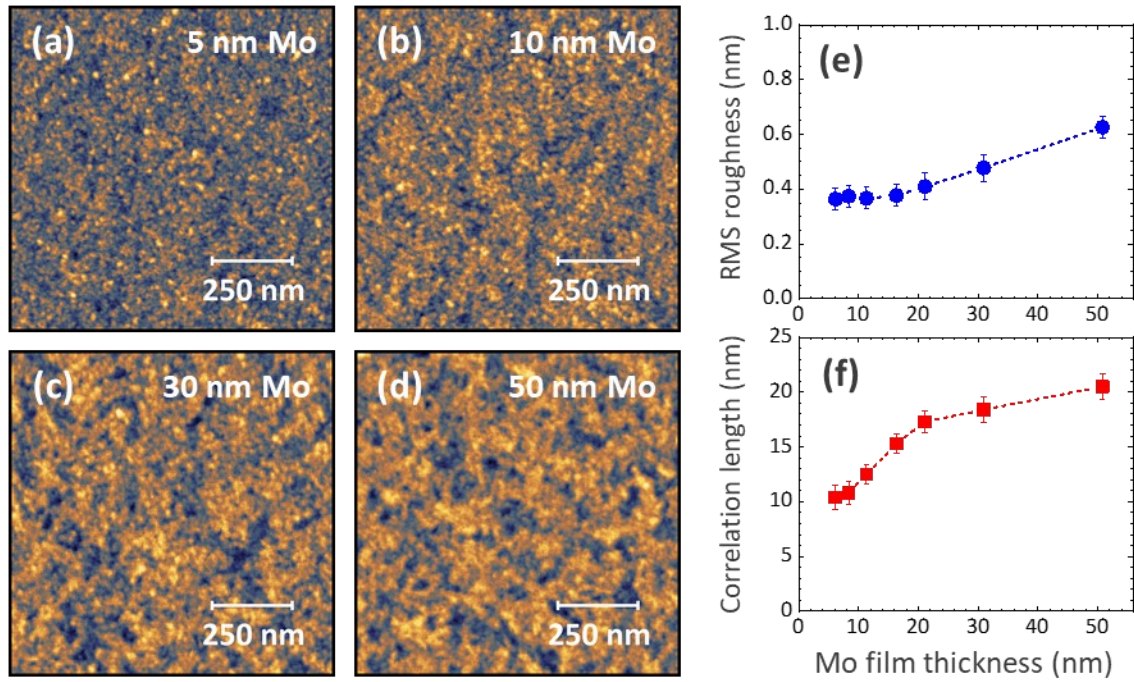
Figure 2: Surface morphology of Mo films: **(a)** to **(d)**: Atomic force micrographs of as deposited Mo thin films on SiO_2/Si with thicknesses as specified. **(e)** RMS surface roughness and **(f)** lateral correlation length deduced from the atomic force micrographs.
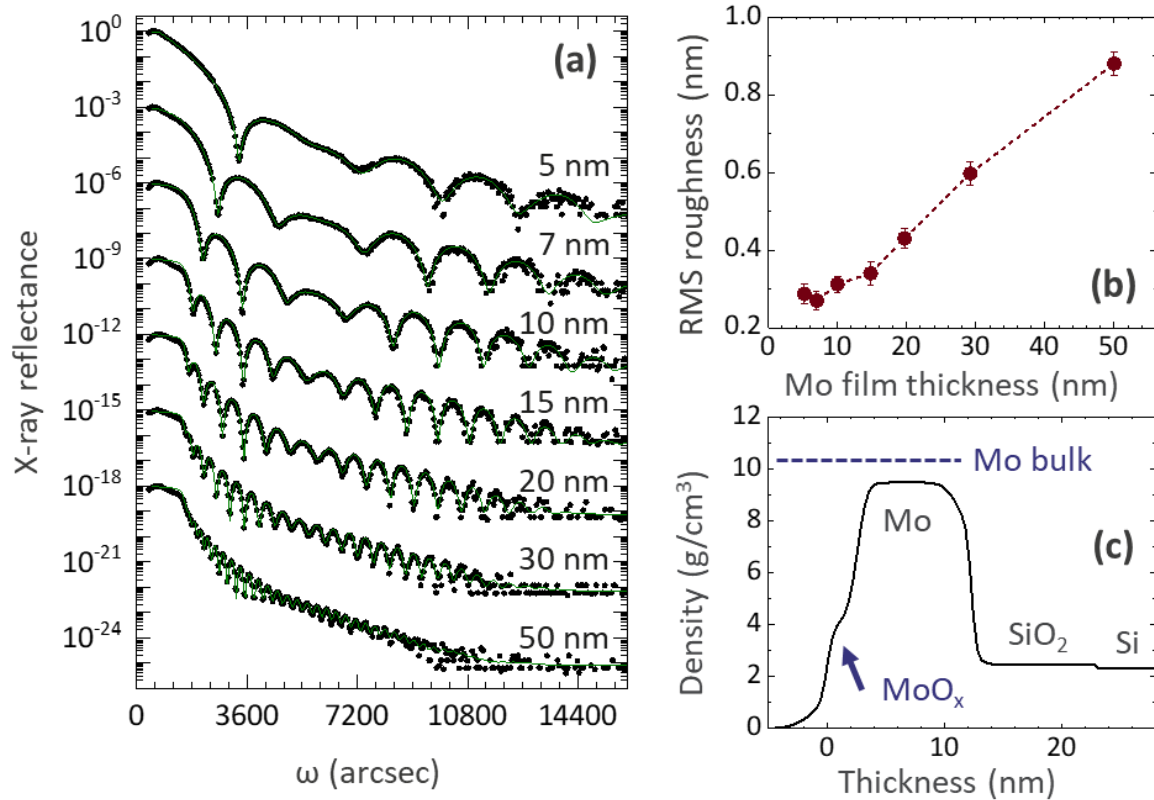
Figure 3: (a) X-ray reflectivity (XRR, black dots) and best fits to the data (green lines) of Mo films with thicknesses as specified. The data are offset for clarity. **(b)** RMS roughness deduced from the XRR data. **(c)** Density profile extracted from XRR of a 10 nm thick Mo film deposited on 10 nm SiO_2/Si.
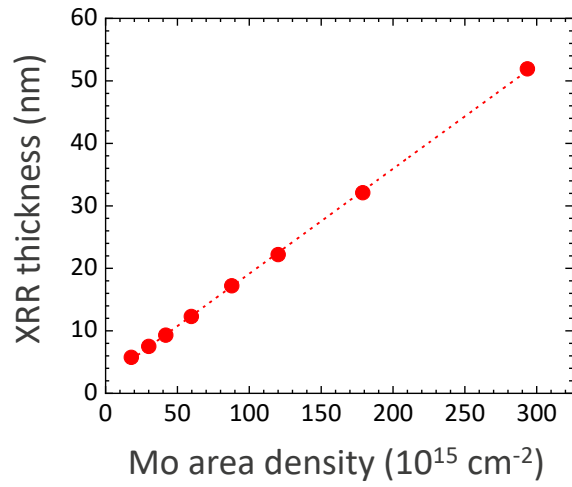
Figure 4: XRR film thickness as a function of the Mo area density measured by RBS. The slope corresponds to a density of 9.7 ± 0.1 g/cm^3, 94% of the bulk Mo density of 10.3 g/cm^3. Error bars are below the size of the symbols.
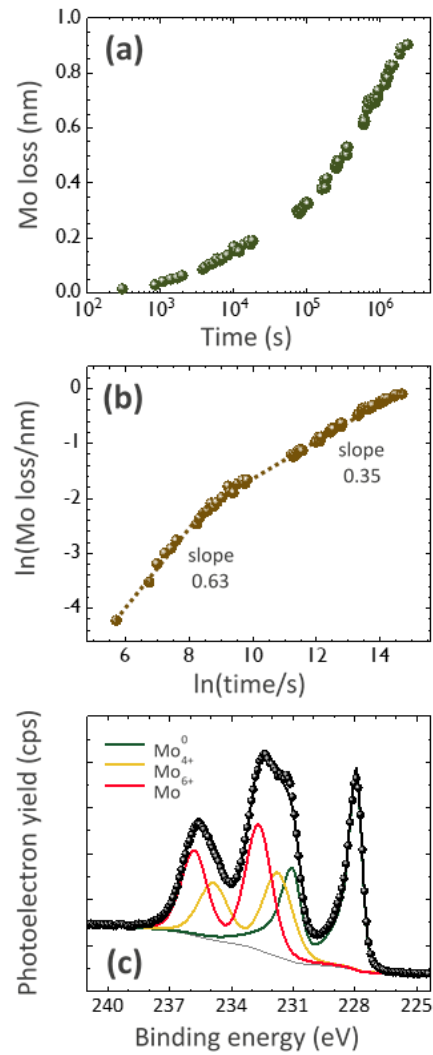
Figure 5: Mo surface oxidation in air: **(a)** Metallic Mo film thickness loss due to surface oxidation deduced from changes of the sheet resistance with air exposure time. **(b)** Double-logarithmic plot of the Mo loss as a function of time indicating two different kinetic regimes. **(c)** Mo 3d XPS spectrum of the Mo surface oxide.
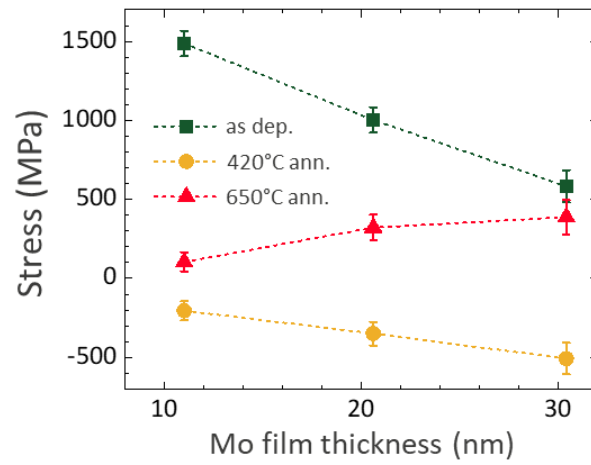
Figure 6: Stress in Mo thin films as a function of their thickness, both as deposited as well as

after annealing at 420ºC and 650ºC in H_2, as indicated.
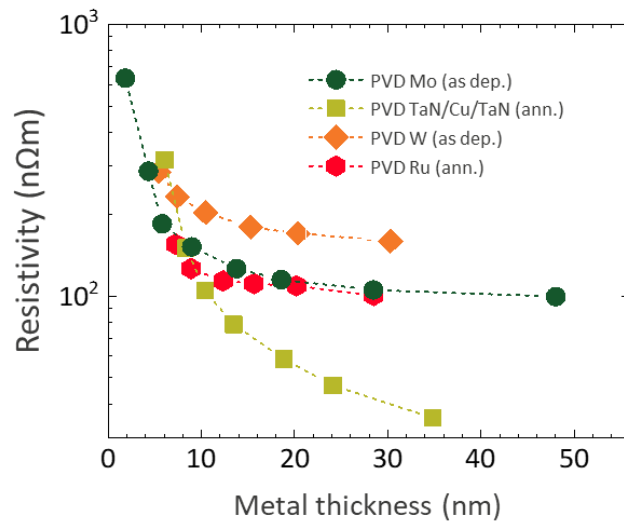
Figure 7: Thickness dependence of the resistivity of as deposited Mo films. As a reference, data are also shown for W, Ru, as well as 1.5 nm TaN/x nm Cu/1.5 nm TaN stacks [27]. The TaN/Cu/TaN and Ru films have been annealed at 420°C in N_2/H_2. Error bars are below the size of the symbols.
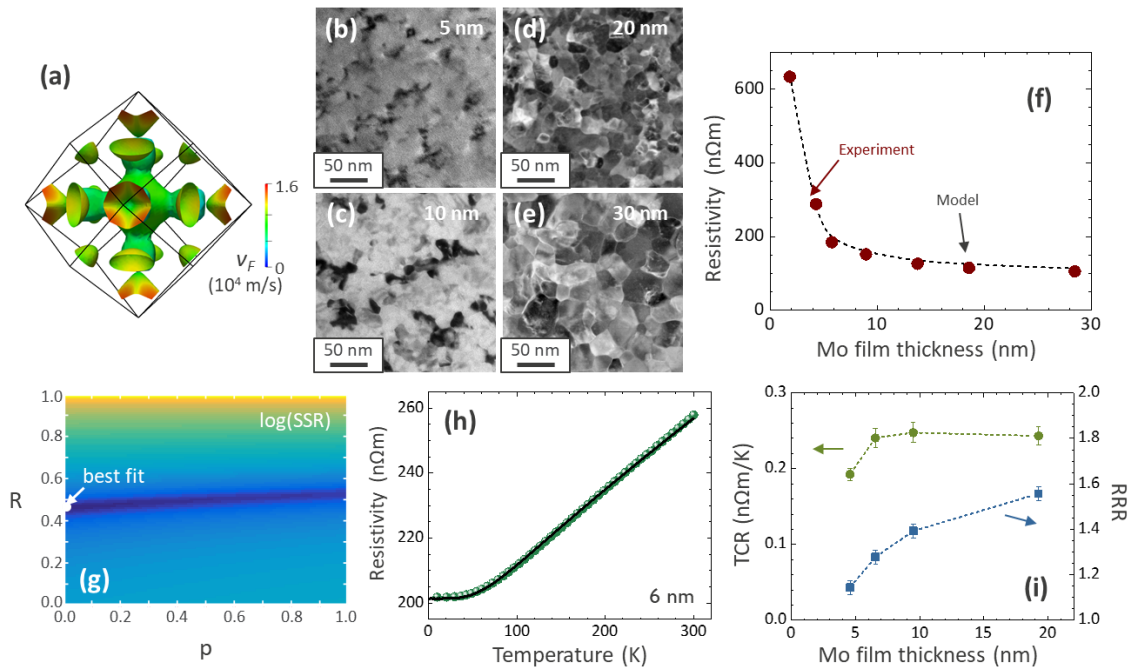
Figure 8: Charge transport in thin Mo films: **(a)** Calculated Fermi surface of bcc Mo. The color scheme represents the Fermi velocity v_F. **(b)** to **(e)** Plan view dark-field transmission electron micrographs of as deposited Mo films with thicknesses as indicated. **(f)** Experimental as well as modelled thickness dependence of the Mo thin film resistivity. The parameters used in the semiclassical Mayadas-Shatzkes model are discussed in the text. **(g)** Sum of squared residuals (SSR, logarithmic color scale) of the model in (f) as a function of surface scattering parameter p and grain boundary scattering parameter R. The position of the best fit in (p, R) parameter space is marked by a white circle. **(h)** Temperature dependence of the resistivity of a 6 nm thick Mo film (dots). The solid line indicates the result of the temperature-dependent Mayadas-Shatzkes model. **(i)** Temperature coefficient of the resistivity (TCR) and residual resistance ratio (RRR) of Mo films as a function of their thickness.
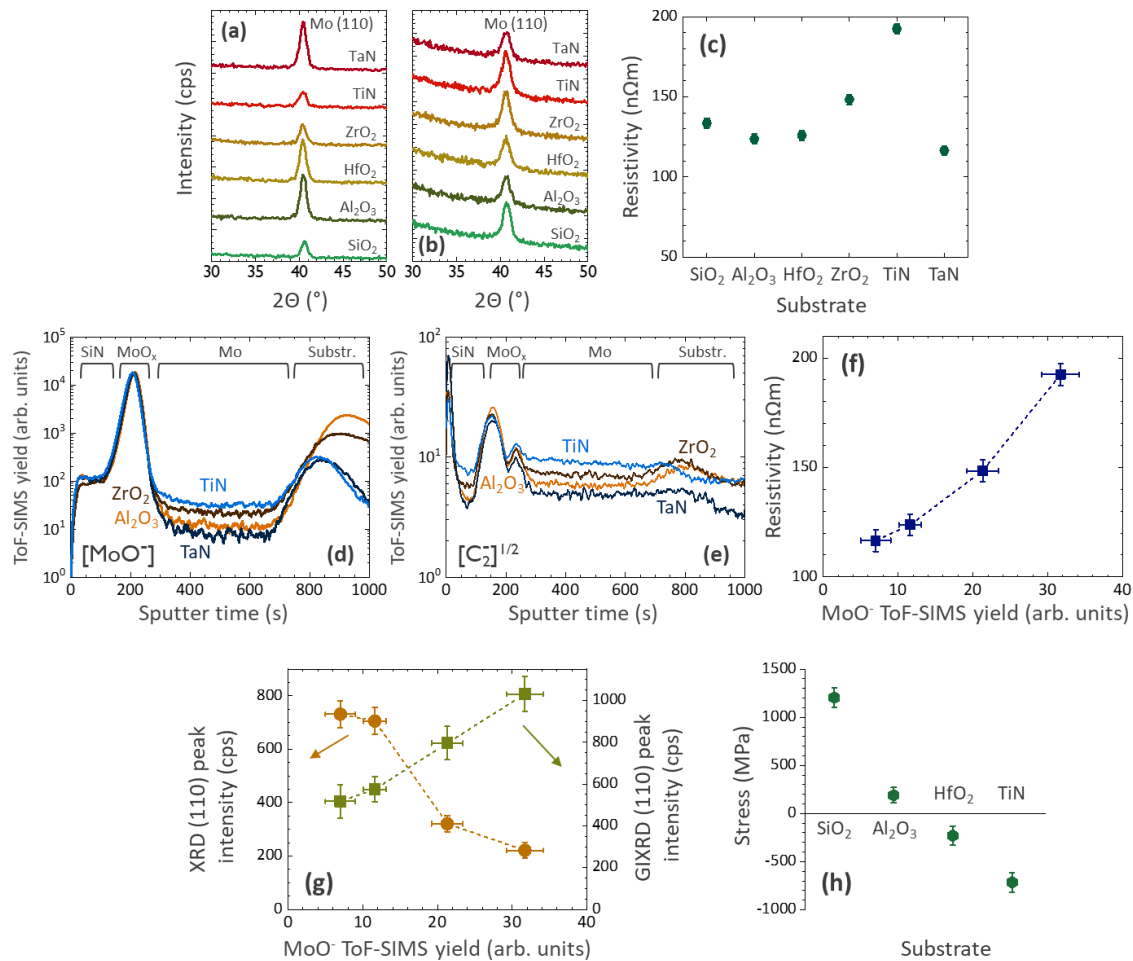
Figure 9: Effect of the substrate on Mo film properties: **(a)** 2θ-ω XRD and **(b)** GIXRD patterns of 15 nm thick as-deposited Mo films on different substrates, as indicated. **(c)** Resistivity of the 15 nm thick Mo films on the different substrates. **(d)** MoO^- and **(e)** C^- (square root of the C_2^- signal) ToF-SIMS yield for 15 nm thick as-deposited Mo films on different substrates, as indicated. **(f)** Resistivity and **(g)** (110) XRD as well as GIXRD peak intensity as a function of MoO^- ToF-SIMS yield for the samples in (d). The O content (MoO^- ToF-SIMS yield) is clearly correlated to resistivity as well as crystallinity. **(h)** Stress in 15 nm thick Mo films on different substrates, as indicated.
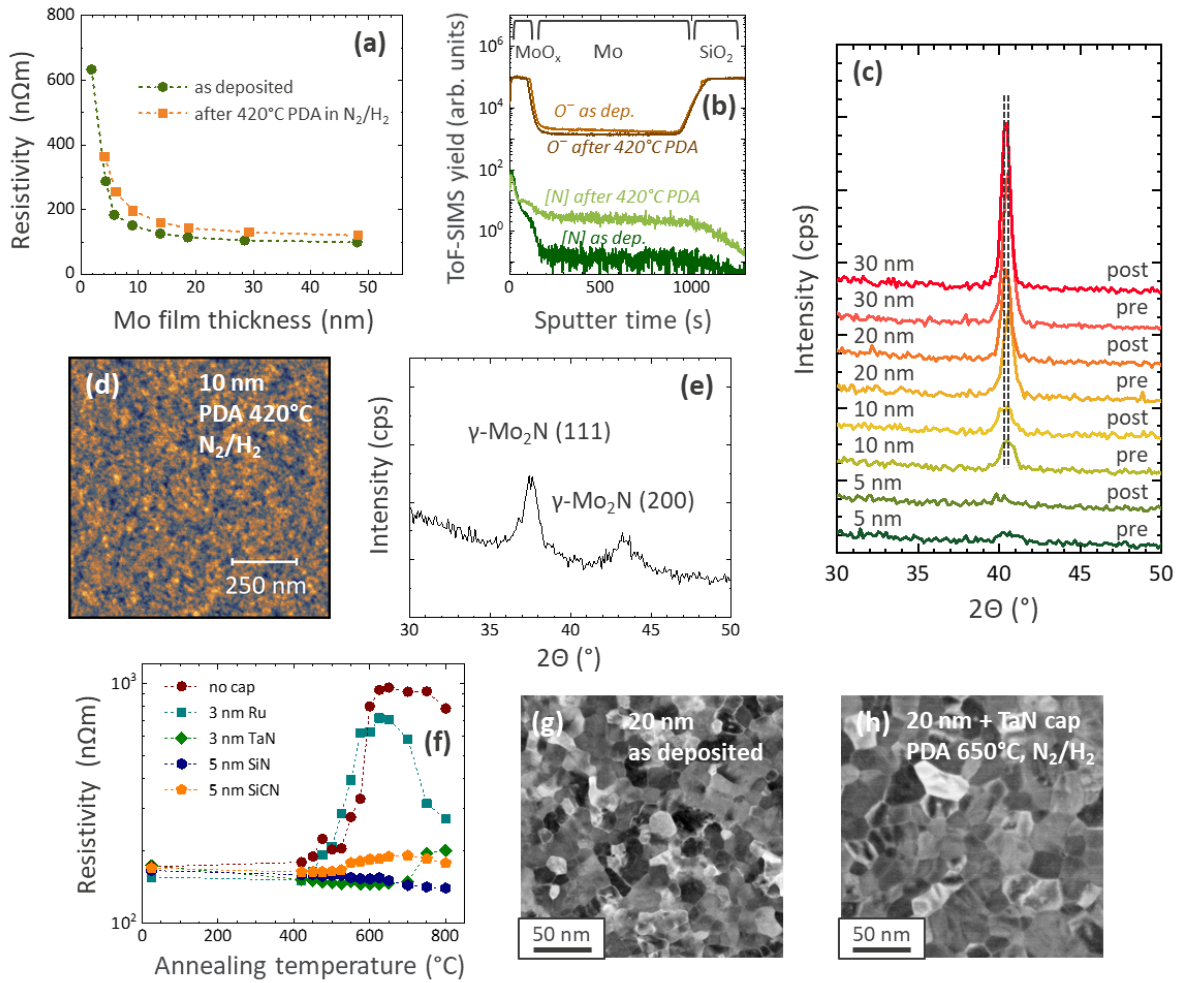
Figure 10: Annealing in N_2/H_2: **(a)** Mo resistivity *vs.* film thickness both as deposited and after annealing at 420°C in N_2/H_2. **(b)** O^- and N ($[CN^-]/[C^-]$) ToF-SIMS yields in 20 nm thick Mo films both as deposited and after a 420°C PDA in N_2/H_2. Error bars are below the size of the symbols. **(c)** 2θ-ω XRD patterns of Mo films with thicknesses as indicated, both pre and post annealing at 420°C in N_2/H_2. **(d)** Atomic force micrograph of a 10 nm thick Mo films after a 420°C PDA in N_2/H_2. **(e)** 2θ-ω XRD pattern of a 20 nm Mo film after a 650°C PDA in N_2/H_2. **(f)** Resistivity of 20 nm thick Mo films as a function of annealing temperature in N_2/H_2 for Mo without and with capping layers as indicated. **(g)** and **(h)** Plan view dark-field transmission electron micrographs of 20 nm Mo films (g) as deposited and (h) with a 3 nm TaN capping after annealing at 650°C in N_2/H_2.
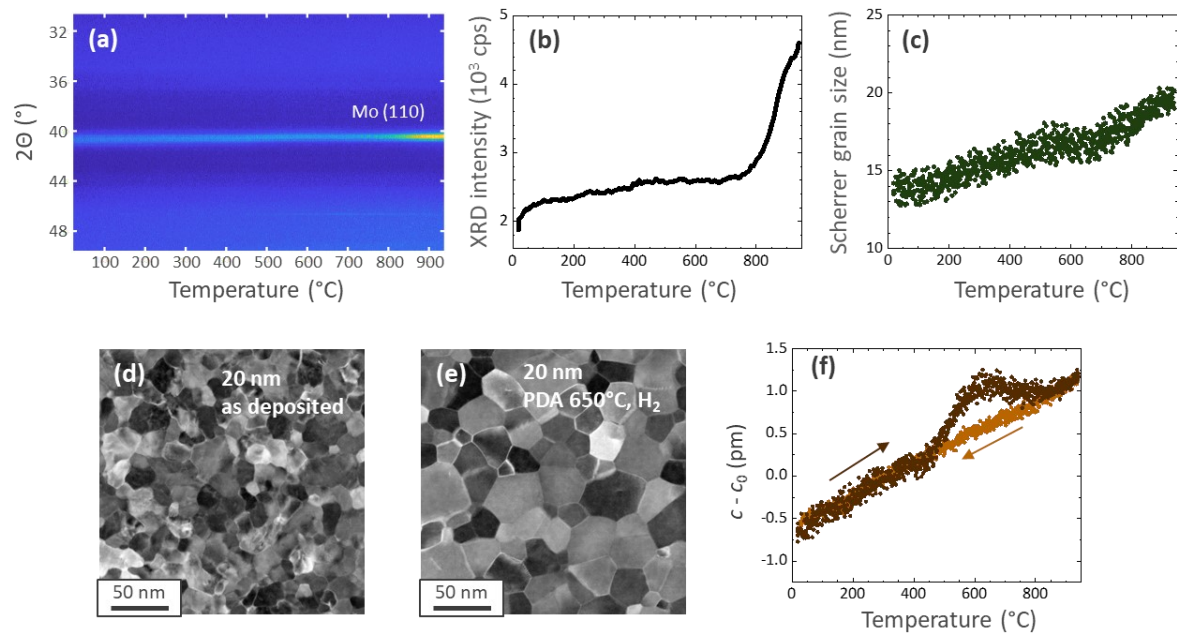
Figure 11: Microstructural evolution during Mo annealing: **(a)** *In situ* 2θ-ω XRD pattern of a 20 nm thick Mo film during ramp annealing in H_2/He between room temperature and 950°C. **(b)** Variation of the Mo (110) XRD intensity and **(c)** of the Scherrer grain size during ramp annealing up to 950°C in H_2/He. **(d)** and **(e)** Plan view dark-field transmission electron micrographs of 20 nm Mo films (d) as deposited and (e) after annealing at 650°C in H_2. **(f)** Variation of the out-of-plane lattice constant c (with respect to the room temperature bulk value c_0) during ramp annealing. Dark brown dots indicate the variation during heating whereas light brown dots correspond to the variation during cooling.